PCCP

Accepted Manuscript

ROYAL SOCIETY OF CHEMISTRY

www.rsc.org/pccp

Submitted to PCCP, 8/21/2014, revised 10/7/2014

Six-dimensional quantum dynamics for dissociative chemisorption of H_2 and D_2 on Ag(111) on a permutation invariant potential energy surface

*Bin Jiang and Hua Guo**

Department of Chemistry and Chemical Biology, University of New Mexico, Albuquerque, NM 87131, USA

* corresponding author: hguo@unm.edu

Abstract

A six-dimensional potential energy surface (PES) for H_2 dissociation on rigid Ag(111) is developed by fitting ~4000 plane-wave density functional theory points using the recently proposed permutation invariant polynomial-neural network (PIP-NN) method, which enforces both the surface periodicity and molecular permutation symmetry. Quantum reactive scattering calculations on the PIP-NN PES yielded dissociative sticking probabilities for both H_2 and D_2. Good agreement with experiment was achieved at high collision energies, but the agreement is less satisfactory at low collision energies, due apparently to the neglect of surface temperature in our model. The dissociation is activated by both vibrational and translational excitations, with roughly equal efficacies. Rotational and alignment effects were examined and found to be quite similar to hydrogen dissociation on Ag(100) and Cu(111).

I. Introduction

The dissociative chemisorption of H_2 on metal surfaces is of fundamental importance in understanding gas-surface reaction dynamics and has been extensively studied both experimentally and theoretically.[1-4] Since hydrogen is much lighter than surface atoms, collision induced phonon and electron-hole pair excitations often play a minor role.[3, 5] As a result, accurate theoretical simulations for the dissociative dynamics can be performed with the Born-Oppenheimer and static surface (BOSS) approximation. Indeed, many quantum dynamical (QD) studies have been carried out on six-dimensional (6D) adiabatic potential energy surfaces (PESs) built on density functional theory (DFT) calculations.[2-4] For instance, excellent agreement between theory and experiment has been achieved for H_2 dissociation on copper surfaces.[4, 6-8]

Earlier experimental evidence suggested that H_2 prefers to adsorb molecularly on silver surfaces,[1, 9-11] suggesting that its dissociative chemisorption is highly activated. On the other hand, the activation energy for recombinative desorption of adsorbed hydrogen atoms was estimated to be relatively low, ranging from 6.4 to 10.5 kcal/mol.[12-15] As a result, the H_2 dissociation on silver is endothermic.[16] Many earlier experiments have thus focused on H_2 scattering from Ag(111)[17-20] or Ag(110)[21] at low collision energies, where the dissociation is negligible. Dissociative sticking probabilities of D_2 on Ag(111) were measured as a function of translational energy for the first time in 1995 by Hodgson and coworkers,[16] followed by a series of dynamical studies on H_2 and D_2 dissociative chemisorption and recombinative desorption on the

same surface.[15, 22-24] These thermal and/or state-specific experimental measurements provided detailed information on vibrational efficacy, surface temperature effects, etc.

In spite of the aforementioned experimental studies, there have been relatively few theoretical studies on the H_2/Ag(111) system until very recently. Earlier quasi-classical trajectory and reduced-dimensional quantum scattering calculations were performed using model PESs.[25-27] The first plane-wave DFT study of the dissociative adsorption of H_2 on Ag(100) was reported in 1997 by Eichler *et al.*,[28] cumulating with a six-dimensional PES. This was followed by full-dimensional quantum dynamics calculations.[29-30] More recently, hydrogen activation on other silver surfaces have been investigated using DFT by several other groups,[31-35] who focused on the effects of crystallographic faces of the silver surface and/or pre-covered oxygen on the activation. Very recently, the effects of hindered rotation on ortho-para H_2 conversion on Ag(111) have been theoretically investigated by Kunisada and Kasai.[36]

The sticking probabilities for H_2/D_2 on Ag(111) computed on a DFT-based PES, which can be directly compared with experimental data of the Hodgson group, have only been reported very recently by us.[37] Using the newly proposed permutation invariant polynomial-neural network (PIP-NN) method, we constructed the first six-dimensional PES for H_2/Ag(111) and performed preliminary QCT calculations for this reaction.[37] Here, we provide details of the PES construction. In addition, we also report extensive QCT and QD results on the dissociative adsorption for H_2 and D_2 on

Ag(111), which are found to be in satisfactory agreement with available state-specific experimental data. Moreover, isotopic, rotational, vibrational, and steric effects are also investigated. The rest of this publication is organized as follows. In Sec. II, details of the PIP-NN PES fitting and single points sampling procedure are presented. In addition, the equations and parameters used in dynamics calculations are also given. Sec. III compares the calculated dissociative sticking probabilities with available experimental data and discusses various factors that influence the reaction. Finally, Sec. IV concludes.

II. Theory

A. Density functional theory calculations

Plane-wave DFT calculations were performed with the Vienna Ab initio Simulation Package (VASP).[38-39] The Ag(111) surface was modeled using a four-layer slab with a separation of 15 Å in the Z direction and a 2×2 (1/4 ML coverage) surface unit cell. The interaction between the ionic cores and electrons was described with the projector-augmented wave (PAW) method,[40] and the Kohn-Sham valence electronic wavefunction was expanded in a plane-wave basis set[41] with a cutoff at 400 eV. The Brillouin zone was sampled with a 4×4×1 Monkhorst-Pack k-points grid mesh.[42] The exchange-correlation effects were described within the generalized gradient approximation (GGA) using the Perdew-Burke-Ernzerhof (PBE) functional.[43] The Methfessel-Paxton method[44] was used with a smearing width of 0.10 eV to extrapolate the total energy to k_BT = 0 eV. All surface atoms were fixed at their

equilibrium positions within a flat surface model. The optimized bulk lattice constant for silver is 4.16 Å, consistent with the experimental value of 4.09 Å and previous theoretical estimates.[31-32]

To explore the minimum energy path (MEP), the transition state (TS) for the dissociative chemisorption of H_2 on Ag(111) was determined by the climbing-image nudged elastic band (CI-NEB) method.[45-46] The saddle point was verified by vibrational frequency analysis, which showed a single imaginary frequency. Extensive convergence tests have been performed and the results are listed in Table I. It can be seen that our choice of parameters, which are computationally inexpensive for the purpose of the PES construction, sufficiently converge the activation energy within roughly 0.02 eV.

B. Potential energy surface

The representation of multi-dimensional PESs using neural networks has been gaining popularity, thanks largely to the small fitting errors.[47-49] The basic structure of feed-forward NNs consists of an input layer, one or more hidden layers, each with a number of interconnected neurons, and an output layer, as shown in Fig. 1. In general, the value of *k*th neuron in the *i*th hidden layer can be expressed as,

$$y_k^i = f_i\left(b_k^i + \sum_{j=1}^{N_{i-1}} w_{jk}^i y_j^{i-1}\right), \quad 1 \le i \le m, \tag{1}$$

where N_{i-1} is the number of neurons in the (*i*-1)th layer; f_i are transfer functions for the *i*th layer; w_{jk}^i are weights connecting the *j*th neurons in the (*i*-1)th layer and the

*k*th neurons in the *i*th layer and b_k^i are the biases of the *k*th neurons of the *i*th layer. The output energy is expressed analogously as a single neuron in the (*m*+1)th layer,

$$E = f_{m+1}\left(b_1^{m+1} + \sum_{j=1}^{N_m} w_{j1}^{m+1} y_j^m \right). \quad (2)$$

In this work, the hyperbolic tangent function was used as the transfer function for the hidden layers and a linear function was used for the output layer. The NNs were trained using the Levenberg-Marquardt algorithm,[50] and the root mean square deviation (RMSD) of the energies in the input data and the fitted energies was chosen as the performance criterion. Prior to training, the data were divided randomly into three sets, namely the training (90%), validation (5%), and test (5%) sets, which enable the early stopping procedure[49] to avoid over-fitting. Two hidden layers were used and the number of neurons in each layer was optimized, leading to the final fit with 20 and 40 neurons in the first and second hidden layers. 50 training processes with different initial guess were performed and the best fit with the smallest overall RMSD including validation and test data sets was saved for dynamics calculations. The NN toolbox in MATLAB was used for the fitting.[51]

The recently proposed permutation invariant polynomial-neural network (PIP-NN) method was used for the H_2/Ag(111) PES. The PIP-NN method for fitting PESs for gas phase and gas-surface reactions has been discussed in detail in our recent publications,[37, 52-53] so it is only briefly outlined here. The essence of the PIP-NN method is to use in the input layer symmetry functions ($\mathbf{G} = \{G_i\}$) in terms of the

original Cartesian coordinates of each atom in the molecule.[48] These symmetry functions are required to enforce the symmetry with respect to translation parallel to the surface as well as permutation symmetry in the molecule if there are identical atoms. To illustrate the method, we start with ten primitive functions of the atomic coordinates to describe the PES between a heteronuclear diatom and an fcc (111) surface as follows,[54]

$$G_1 = \cos(\frac{4\pi y_1}{a\sqrt{3}}) + 2\cos(\frac{2\pi x_1}{a})\cos(\frac{2\pi y_1}{a\sqrt{3}}), \quad (3)$$

$$G_2 = \sin(\frac{4\pi y_1}{a\sqrt{3}}) - 2\cos(\frac{2\pi x_1}{a})\sin(\frac{2\pi y_1}{a\sqrt{3}}), \quad (4)$$

$$G_3 = \exp(-\lambda z_1), \quad (5)$$

$$G_4 = \cos(\frac{4\pi y_2}{a\sqrt{3}}) + 2\cos(\frac{2\pi x_2}{a})\cos(\frac{2\pi y_2}{a\sqrt{3}}), \quad (6)$$

$$G_5 = \sin(\frac{4\pi y_2}{a\sqrt{3}}) - 2\cos(\frac{2\pi x_2}{a})\sin(\frac{2\pi y_2}{a\sqrt{3}}), \quad (7)$$

$$G_6 = \exp(-\lambda z_2), \quad (8)$$

$$G_7 = \exp(-\lambda r), \quad (9)$$

$$G_8 = \cos(\frac{4\pi Y}{a\sqrt{3}}) + 2\cos(\frac{2\pi X}{a})\cos(\frac{2\pi Y}{a\sqrt{3}}), \quad (10)$$

$$G_9 = \sin(\frac{4\pi Y}{a\sqrt{3}}) - 2\cos(\frac{2\pi X}{a})\sin(\frac{2\pi Y}{a\sqrt{3}}), \quad (11)$$

$$G_{10} = \exp(-\lambda Z). \quad (12)$$

As depicted in Fig. 2, the coordinate origin is placed at a surface atom in the top layer and x axis lies along the two nearest surface atoms. (x_i, y_i, z_i) are Cartesian coordinates for atom i, (i=1 or 2), (X, Y, Z) are Cartesian coordinates for the molecular center of mass (COM). r is the internuclear distance in the molecule, λ is a positive parameter (λ=1.0 Å^{-1} here) ensuring the correct asymptotic behavior for the PES when the molecule is far away from the surface, and a is the distance between two nearest surface atoms (a=2.94 Å for Ag(111)) and is sometimes referred as surface lattice constant. These ten primitive terms incorporate the translational symmetry via the Fourier terms of the lateral coordinates and are sufficient for a heteronuclear diatom/surface system. The permutation symmetry for a homonuclear diatom/surface system can be subsequently introduced by low ordered PIPs[55-56] of the primitive functions. Particularly, we include nine PIPs up to total degree of two in place of six primitive terms (G_1 to G_6):[37]

$$G_{11} = G_1 + G_4, \quad (13)$$

$$G_{12} = G_1 G_4, \quad (14)$$

$$G_{13} = G_2 + G_5, \quad (15)$$

$$G_{14} = G_2 G_5, \quad (16)$$

$$G_{15} = G_3 + G_6, \quad (17)$$

$$G_{16} = G_3 G_6 , \quad (18)$$

$$G_{17} = G_1 G_2 + G_4 G_5 , \quad (19)$$

$$G_{18} = G_1 G_3 + G_4 G_6 , \quad (20)$$

$$G_{19} = G_2 G_3 + G_5 G_6 . \quad (21)$$

Note that G_7 to G_{10} remain unchanged with the exchange of two identical atoms. As discussed in our recent work,[37] thirteen permutationally symmetrized functions, namely G_7 to G_{19}, guarantee the correct translational symmetry and permutation invariance in this six-dimensional PES. An important advantage of PIP-NN is its systematic adaption of the full symmetry for molecule-surface reactions, thus avoiding possible unphysical symmetries and numerical errors in other symmetry adaptation schemes. Specially, we emphasize that the last three PIP cross terms (G_{17} to G_{19}) are necessary to avoid oversymmetrization.[37] It is also noted that this approach is not unique, and different and/or higher-order PIPs can be used for the NN fitting, as long as they provide adequate enforcement of the correct permutation.

The sampling procedure is also important for a high quality and efficient fit of the PES. An ideal data set should contain fewest points but describe accurately the dynamically relevant regions. The sampling was performed iteratively. Starting from an initial set of data along the MEP for the reaction, a primitive PES was first generated. Additional points were generated by running classical trajectories on the primitive PES. These classical trajectories, which are computationally inexpensive

and mainly follow the reaction pathway, were used to explore the dynamically important configurations.[57] New points from these trajectories were added based on both geometric and energetic criteria. This iterative approach generates additional data points in each iteration, leading to the final convergence of the PES.

The energy criterion, which compares energy RMSDs of several NN fitted PESs at a new geometry, accepts the new point if the RMSDs are large, because it suggests a large uncertainty at this point.[48] The geometry criterion is often based on a generalized Euclidean distance between two points, defined for example as the RMSD of bond distances, *i.e.* $d_{mn} = \sqrt{\sum_{i}^{nbond} \left(r_i^m - r_i^n \right)^2}$, where r_i^m and r_i^n are the *i*th bond lengths in *m*th and *n*th points.[58] For a molecule-surface system, however, bond distances are not good coordinates due to surface periodicity, and the permutation symmetry further complicates this issue. Instead, symmetry functions as the input of the NNs offer a better choice.[54] Indeed, the build-in periodic symmetry describes the "closeness" between two points in a single unit cell as well as in different periodical units. Within our PIP-NN framework, mirror images via permutation operations of identical atoms can also be recognized. Unlike the bond distance in gas phase systems, however, it is necessary to normalize the PIPs before evaluating the generalized Euclidean distance, as their numerical ranges can be very different. One can easily estimate the maximum ($G_{i,\max}$) and minimum ($G_{i,\min}$) of a PIP using the first few hundred points in the initial data set. The generalized Euclidean distance between the *m*th and *n*th points in the H_2/Ag(111) system is hence expressed as

$d_{mn} = \sqrt{\sum_{i=7}^{19}\left(\bar{G}_i^m - \bar{G}_i^n\right)^2}$ where $\bar{G}_i^m$ and $\bar{G}_i^n$ are the *i*th normalized PIPs in two points, e.g. $\bar{G}_i = \left(G_i - G_{i,\min}\right)/\left(G_{i,\max} - G_{i,\min}\right)$. Note that the $G_{i,\max}$ and $G_{i,\min}$ are updated after every new point added. We note in passing that this criterion is also applicable to PES construction for gas phase systems.

C. Quasi-classical trajectory method

QCT calculations were performed using the VENUS code[59] modified for studying molecule-surface collision dynamics by us. The trajectories were initiated with H_2 above the Ag(111) surface (Z=8.0 Å) and the internal coordinates and conjugate momenta of the diatomic molecule were sampled semi-classically for given vibrational and rotational quantum numbers n and j.[60] Only the ground ro-vibrational state (n=0, j=0) was considered in this work as QCT calculations were primarily used to confirm the convergence of the PES fitting. The initial (X, Y) coordinates of the H_2 COM was randomly chosen in the unit cell, as well as the initial polar and azimuthal angles (θ, φ). Only the normal incidence was studied with the momentum defined by the translational energy in the Z direction.

The trajectories were integrated by a combined 4th-order Runge-Kutta and 6th-order Adams-Moulton predictor-corrector methods and the propagation time step was selected to be 0.10 fs. Numerical gradients were computed with the differential of 0.0001 Å. All trajectories conserved energy within 0.1 meV. In total, 3000-10000 trajectories were calculated depending on the translational energy. The molecule was

considered dissociated on the surface when the H-H distance is larger than 2.5 Å, while non-reactive if it is scattered back beyond 8.1 Å above the surface. The dissociation probability was evaluated as the ratio of reactive trajectories (N_r) and total trajectories (N_t), $P_r = N_r/N_t$.

D. Quantum dynamical method

Within the Born-Oppenheimer and static surface (BOSS) approximation, the six-dimensional quantum dynamics was studied by a time-dependent wave packet method. The Hamiltonian ($\hbar$=1) for the title reaction is described with six coordinates (u, v, Z, r, θ, φ) as depicted in Fig. 2,[61]

$$\hat{H} = -\frac{1}{2M}\frac{\partial^2}{\partial Z^2} - \frac{1}{2\mu}\frac{\partial^2}{\partial r^2} + \frac{\hat{j}^2}{2\mu r^2} + V(u,v,Z,r,\theta,\varphi) - \frac{1}{2M\sin^2\alpha}\left(\frac{\partial^2}{\partial u^2} - 2\cos\alpha\frac{\partial^2}{\partial u\partial v} + \frac{\partial^2}{\partial v^2}\right), \quad (22)$$

where M and μ are the total mass and reduced mass of the diatom, $\hat{j}$ is the angular momentum of the diatom, u and v are the non-orthogonal lateral coordinates along the lattice axes crossed with a skew angle α of 60° for Ag(111) in order to take advantage of the surface periodicity, Z is the distance between the diatomic COM and the surface, r is the diatomic bond length, θ is the polar angle between r and the surface normal, and φ is the azimuthal angle.

The wave function was expanded in a finite basis representation (FBR) consisting of the translational basis in Z, vibrational basis in r, rotational basis in (θ,φ), and Fourier basis in u and v. Following Dai and Light,[61] the wave functions for u and v

were represented by the periodic Fourier functions $exp(ik_u u)$ and $exp(ik_v v)$. Their coordinate representations correspond to even spaced Fourier grids and the transformation to and from the FBR can be readily evaluated by fast Fourier transform (FFT).[62] Sine basis functions were used for the translational coordinate Z,[63] which is divided into the interaction and asymptotic regions, in order to take advantage of an L grid saving scheme,[64]

$$\chi_{n_Z}(Z) = \sqrt{\frac{2}{Z_{\max} - Z_{\min}}} \sin \frac{n_Z \pi (Z - Z_{\min})}{Z_{\max} - Z_{\min}}, \text{ for asymptotic region,} \quad (23)$$

$$\chi_{n_{Z'}}(Z) = \sqrt{\frac{2}{Z_{\text{int}} - Z_{\min}}} \sin \frac{n_{Z'} \pi (Z - Z_{\min})}{Z_{\text{int}} - Z_{\min}}, \text{ for interaction region.} \quad (24)$$

Here $Z_{\min}$ and Z_{int} define the boundaries of the interaction region, while $Z_{\min}$ and $Z_{\max}$ correspond to the boundaries of the asymptotic region. The vibrational basis in r consists of the eigenfunctions $\phi_n(r)$ for the one-dimensional reference Hamiltonian for the isolated diatom far from the surface, which satisfies the equation,

$$\left[-\frac{1}{2\mu} \frac{\partial^2}{\partial r^2} + V_r(Z_\infty, r) \right] \phi_n(r) = \varepsilon_n \phi_n(r). \quad (25)$$

In the asymptotic region, only energetically open and a few closed vibrational channels were included, resulting in significant savings. In the interaction region, on the other hand, a larger number of vibrational basis was needed to allow diatomic dissociation. A non-direct product FBR consisting of spherical harmonics $Y_j^{m_j}(\theta, \varphi)$ was employed to represent the angular wave function. The corresponding angular grid is a direct product of the Gauss-Legendre quadrature points in θ and a Fourier grid in

φ, and two one-dimensional pseudo-spectral transformations can easily convert the FBR to and from the grid.[65-67]

The initial normal-incident wavepacket was chosen as,

$$\psi(t=0) = NG(Z)\phi_n(r)Y_j^{m_j}(\theta,\varphi), \tag{26}$$

where $G(Z)$ is the normalized Gaussian function along the surface normal,

$$G(Z) = (\pi\delta^2)^{-1/4}\exp\left(-\frac{(Z-Z_0)^2}{2\delta^2}\right)\exp(-ikZ), \tag{27}$$

and (n, j, m_j) are vibrational, rotational, and magnetic quantum numbers for the initial state of the diatom, N is the normalization constant that equals $1/a$ in this fcc case. The wave vector k is determined by the translational energy E_t: $k = \sqrt{2ME_t}$, Z_0 and δ are the initial central position and width of the Gaussian wave packet. The wave function was propagated using the split-operator method[68] and absorbing potentials were imposed at the edges of the grid to avoid spurious reflections,

$$D(\zeta) = \exp\left[-C_\zeta\left(\frac{\zeta-\zeta_a}{\zeta_{\max}-\zeta_a}\right)^2\right], \quad \zeta = Z \quad or \quad r. \tag{28}$$

The initial state-selected dissociation probability was obtained by evaluating the energy dependent reactive flux at the dividing surface ($r = r_f$), namely,

$$P_{n_0,j_0,m_{j0}}(E) = \frac{1}{\mu}\mathrm{Im}\left\langle\psi_{iE}^+\middle|\delta(r-r_f)\frac{\partial}{\partial r}\middle|\psi_{iE}^+\right\rangle_{r=r_f}, \tag{29}$$

where Im means the imaginary part, $|\psi_{iE}^+\rangle$ is the time-independent wave function

which can be obtained by Fourier transform of the time-dependent wave function $\psi(t)$ over time:

$$\left|\psi_{iE}^{+}\right\rangle = \frac{1}{a_i(E)}\int_0^\infty e^{iEt}\left|\psi(t)\right\rangle dt\,, \tag{30}$$

where the coefficient $a_i(E)$ is the overlap between the initial wavepacket $\psi(t=0)$ and the energy-normalized asymptotic scattering function ϕ_{iE}.

Although the approach outlined above bears many similarities with existing wave-packet based methods, there are several technical differences. For example, our implementation differs from that of Dai and Light[61] and Liu *et al.*[69] in using a non-direct product basis for (θ,φ) instead of the approximately separated direct product representation of the angular momentum operator. On the other hand, we obtain the dissociation probability by a direct flux method, which is different from the scattering amplitude method used by Kroes and coworkers.[3] The parameters used in quantum dynamics are listed in Table II. Note that the number of basis for the rotationally and/or vibrationally excited states is slightly larger.

III. Results and Discussion

A. Density functional theory calculations

The weak interaction between molecular hydrogen and Ag(111) features a shallow physisorption well, which lies at 4.01 Å above the surface with a well-depth of roughly 0.007 eV. This is in good agreement with the findings of Montoya *et al.*,[32]

who reported a physisorbed H_2 well at 3.8 Å above the surface with the small adsorption energy of ~ 0.017 eV. The shallowness of the well should be considered with caution as the DFT is known to describe dispersion poorly. On the other hand, the most stable adsorption site for the H atom is the fcc site with a binding energy of 2.07 eV, again comparing well with the previously reported values.[31-32] The most favorable co-adsorbed state, in which the two chemisorbed hydrogen atoms are at the two nearest fcc sites, is referred as "fbf" hereafter, while a local minimum that directly connects with the transition state is referred as "fbh", with two chemisorbed H atoms at adjacent fcc and hcp sites. In the subsequent CI-NEB calculations, the initial state (IS) was selected as the shallow physisorption well, where either the fbf or fbh site was chosen as the final state (FS). Both cases led to the same transition state (TS). Five images were employed to locate the TS, which is the energetically highest image along the MEP. The reaction path along with the geometries of stationary points is shown in Fig. 3.

The TS at the bridge site features a H-H distance elongated to 1.26 Å and an energy of 1.16 eV relative to H_2 being far away above the surface. The geometry and barrier height are in excellent agreement with those obtained in earlier DFT calculations.[31-32] In addition, the dissociation of H_2 was found to be endothermic by 0.47 eV, consistent with experimental observations ($\geqslant$0.52 eV).[16]

It is interesting to compare with the dissociation of H_2 on Ag(100), which also has a high and late barrier. In particular, the H-H bond at the transition state at the hollow

site is elongated to 1.37 Å with a barrier height of 1.10 eV,[28] comparing to 1.26 Å and 1.16 eV on the Ag(111) surface at the bridge transition state. Both cases have "later" barriers than H_2 dissociation on Cu(111), which has a H-H distance of 1.10 Å at the transition state.[6] The late barriers in these processes suggest a higher vibrational efficacy in promoting the dissociation according to Polanyi's Rules.[70]

B. Potential energy surface

Our data set started with about 800 configurations randomly sampled near the MEP. Special care was taken to avoid unreasonable geometries, where either two hydrogen atoms are too close or a hydrogen atom is too close to the surface. The PIP-NN fitting resulted in a primitive PES. A few thousand classical trajectories were then dispatched on this PES to generated additional geometries. For each candidate geometry, we evaluated RMSDs in energy and geometry as discussed above. A point was added to the data set if its generalized Euclidean distances from all existing data points are larger than 0.1 and energetic RMSDs are larger than 0.8 kcal/mol. An improved PES was then obtained from this updated data set via a new PIP-NN fit, and the procedure was repeated until no new point can be added and/or the dynamical results converged. Note that fewer points were added in the first few iterations, as the PES was insufficiently accurate and the sampled points were not optimal. As the number of points in the data set increases, the fitted PES becomes more accurate and more sampling points can be collected. Overall, 3431 points were selected to obtain a converged PES with respect to QCT dissociation probabilities, while 4016 points

were finally used to obtain well-converged quantum dissociation probabilities and to remove unphysical holes in regions far from the MEP. Unlike the recent work on the NN PES of the HCl/Au(111) system,[71] our PIP-NN PES achieves about the same accuracy in terms of fitting error with far less DFT points and a single NN fit, rather than four fits connected with switching functions.

After some tests on the number of neurons in each layer, the final choice of the NN structure contains 20 and 40 neurons in the two hidden layers, as well as 13 PIPs in the input layer, resulting in 1161 parameters in total. Further increases of the number of parameters did not result in meaningful improvement in the quality of the fit. A total RMSD of merely 2.5 meV was finally obtained using this 13-20-40 NN structure with the 4016 points, with a maximum error of only about 33.6 meV. It should be noted that the points in the validation and testing sets, which have been selected randomly and not included in the fitting, were included in the overall RMSD evaluation, RMSDs for training/validation/test sets are 2.0, 4.7, and 5.5 meV respectively. Indeed, the PIP-NN method is comparable in fitting accuracy to the corrugation reducing procedure (CRP) method,[72] which is recognized as the most accurate PES construction method for diatom-surface systems.

We further checked the accuracy of our PIP-NN PES representation of the MEP. To this end, the MEP from the physisorption well to the fbh (fbf is energetically lower but not the one directly connecting the saddle point) site was first obtained based on PIP-NN PES, and corresponding geometries along the reaction coordinate were

extracted and computed directly with DFT. As seen in Fig. 4, the new DFT energies, which were not used in the fitting, perfectly match the fitted energies. In addition, the fitted and DFT calculated barrier height and frequencies at TS also agree well, as noted in the same figure, confirming the accuracy of the PIP-NN PES.

In Fig. 5, contour plots of the PES at the top (X=0 and Y=0), bridge (X=a/2 and Y=0), and fcc (X=0 and $Y=\sqrt{3}a/3$) sites are shown as a function of Z and r, with θ and φ optimized. There exists a saddle point in each contour plot and the lowest barrier is the one at the bridge site, consistent with the CI-NEB calculation. On the other hand, the barrier height at the top and fcc sites are both higher than the global barrier height by roughly 0.3 eV. Although the hcp and fcc sites are distinguishable in our symmetry functions, the contour plot at the hcp site is quite similar to that at the fcc site, and is thus not shown. Another important feature from these contour plots is that the PES does not suffer from the problem of unphysical holes and the dynamically relevant areas are well represented.

To check the dynamical convergence with respect to the number of DFT points, we have performed both QCT and QD calculations based on three best PESs obtained from the last three iterations, and the results are plotted in Fig. 6. It is clearly that both QD and QCT dissociation probabilities for the ground ro-vibrational state of H_2 are nicely converged with regard to the number of points. In addition, the QCT probabilities show a similar threshold and translational energy dependence as the QD counterparts, although the former slightly overestimate by approximately 10%-20%,

presumably due to leakage of the zero-point energy.

C. Quantum dynamics

Taking advantage of the detailed balance, Hodgson's group have measured several state-specific sticking coefficients for H_2 and D_2 by means of the (2+1) resonance enhanced multiphoton ionization (REMPI) technique.[16, 22-23] The experimental sticking coefficients reach as low as 10^{-9}, presenting a daunting challenge for theoretical simulations. In addition, the surface temperature significantly enhance the dissociation at low collision energies, but has essentially no effect on the reaction at high collision energies.[23] Since the BOSS approximation in our QD calculations ignores surface temperature effects, our theoretical model is not expected to reproduce the extremely small sticking coefficients at very low energies. However, the sticking coefficients at high energies are less influenced by the surface motion and should be described well by our theory. This is indeed the case, as the comparison between the calculated and measured results for $H_2(n=0,j=3)$, $D_2(n=0,j=2)$, and $D_2(n=1, j=2)$ is shown in Fig. 7. Note that the former were obtained with averaging over the $(2j+1)$ m_j state. As expected, the agreement of theory and experiment is good at high translational energies, but theory largely underestimates sticking coefficients at low energies, due largely to the neglect of surface effects. Another source of disagreement may arise from the condition under which the experimental sticking coefficients[16, 22-23] were derived from the recombinative desorption measurements by scaling S_0 to unit at the largest accessible translational energy, which is not completely true. Recent

studies on the methane[73] and hydrogen dissociation[74] on various metal surfaces have shown that lattice motion can significantly assist the dissociation at low energies. However, previous theoretical studies on H_2 dissociative chemisorption have seldom focused on the energy range below the static barrier height.

Interestingly, the experimentally measured vibrational efficacy for D_2(n=0, j=2) to D_2(n=1, j=2) is well reproduced by our QD results. Here, we define the vibrational efficacy as $\eta = \frac{E_T(0,S_0) - E_T(n,S_0)}{\Delta E_n}$, where ΔE_n is the vibrational excitation energy for $0 \rightarrow n$ and $E_T(0,S_0) - E_T(n,S_0)$ is the translational energy difference for a given sticking coefficient between the ground and nth vibrational states. Indeed, the excitation to the first vibrationally excited state of D_2 promotes the dissociation significantly and its efficacy is nearly as large as the same amount translational energy. For example, at the same sticking coefficients of 10^{-3}, the measured translational energy difference between n=0 and n=1 results is about 0.329 eV,[23] while the calculated translational energy difference is about 0.334 eV, leading to experimental and theoretical vibrational efficacies of 0.89 and 0.90, respectively, given the vibrational excitation energy of 0.371 eV for D_2(n=0→1).[23] In addition to this excellent agreement, both experimental and calculated results show that the translational energy spacing between n=0 and n=1 state hardly changes in a large range of translational energy, validating the S curve proposed by Luntz.[75]

It is interesting to compare the vibrational efficacy in this case to that in H_2/Cu(111) system. The vibrational efficacy for D_2(n=1) on Cu(111) surface was

found to be about 0.58,[7, 76] much lower than 0.90 on Ag(111) here, which can presumably be attributed to the fact that the TS of H_2 dissociation on Ag(111) is "later" than that on Cu(111). Nonetheless, vibrational efficacies of less than unity in both reactions imply that the vibrational energy is less effective than the same amount of translational energy in promoting the reaction, which seems to be in contrary to the prediction of Polanyi's rules.[70]

To provide a more quantitative measure of the vibrational efficacy, we explored the coupling of the reactant modes with the reaction coordinate at the transition state, using our recently proposed Sudden Vector Projection (SVP) model.[77-78] The basic premise of the SVP model is that the collision time is often shorter than the time required for energy flow within the reactant. In this sudden limit, the coupling of a reactant mode with the reaction coordinate at the transition state can be approximately quantified by the projection of the reactant normal mode vector ($\vec{Q}_i$) onto the reaction coordinate vector ($\vec{Q}_{RC}$): $\eta_i = \vec{Q}_i \cdot \vec{Q}_{RC} \in [0,1]$. This SVP model has been successfully applied to the dissociative chemisorption of both methane[79-81] and water,[82] and should be applicable to the current reaction. Indeed, the calculated SVP values (η_i) for the *X*, *Y*, *Z* and D_2 vibrational modes are 0.01, 0.01, 0.40, and 0.92. The small SVP values for *X* and *Y* translational modes and the large value for Z are consistent with the normal scaling of this reaction.[24] On the other hand, the rather large SVP value for the vibrational mode is a bit deceiving as the bridge saddle point was used in the SVP calculation. As shown in Fig. 5, reaction can take place at other sites with slightly higher barriers, but these sites all have different orientations of the D_2 moiety. Since

the D_2 moiety at the reactant asymptote was optimally aligned with that at the bridge saddle point in the SVP calculation, it has inevitably poor alignments with the D-D orientations at other sites. Furthermore, the model excludes other less well aligned reactant geometries with different polar and azimuth angles, which could also dissociate but have smaller SVP overlaps. As a result, the SVP value for the vibration of D_2 represents an overestimation and can only be considered as the upper limit of the vibrational effect. Nonetheless, the large value is consistent with the large vibrational enhancement.

Figure 8 compares the QD sticking coefficients for H_2 and D_2 at several ro-vibrational states. The ground state H_2 is moderately more reactive than ground state D_2, which is consistent with the slightly lower zero point energy (ZPE) corrected barrier height 1.08 eV for H_2 than 1.10 eV for D_2. The threshold for H_2 dissociation is slightly lower than that for D_2 dissociation, and both are lower than their ZPE corrected barrier heights, suggesting some tunneling. Interestingly, for both isotopes, low rotational excitations do not change the reactivity much, while vibrational excitation greatly enhances the reaction. We will focus on D_2 below as it has been more frequently investigated by experimentalists.

The effect of higher rotational excitations is examined in Fig. 9 up to j=11 for the vibrationally ground state D_2. Note that the j-dependent dissociation probabilities here have been averaged over m_j. Similar to H_2 dissociation on Cu(111)[7, 61] and Cu(100),[83] excitations to low rotational states (j<3) have little impact on the reactivity, while the

higher rotationally excited states enhance the reaction. The rotational effects have been interpreted by Darling and Holloway for the H_2/Cu(111) system:[84] The low rotational excitations reduce the possibility for the adsorbate to approach the transition state, while the further increasing in rotational energy, on the other hand, can couple into the reaction coordinate thus promote the reaction. Given the similarities between these two systems, it is expected that the same mechanism is in operation here.

Figure 10 shows the difference in the dissociation probability for each m_j state of (n=0, j=5). It is found that the sticking probability increases monotonically with m_j. Indeed, the transition state at bridge site features H_2 parallel to the surface, thus favoring the $m_j = j$ state, which rotates classically like a "helicopter". On the other hand, the $m_j = 0$ state behaves classically like the "cartwheel", thus disorienting the molecule away the preferable transition state and inhibiting the dissociation. This phenomenon has been widely observed in other H_2 dissociative reactions with a similar transition state that lies parallel to the surface plane.[8, 61]

The experimentally measurable rotational alignment parameters $A_0^{(2)}$, which can be expressed by the m_j dependent dissociative probabilities, e.g. $A_0^{(2)}(E)= \sum_{m_j=-j}^{j} \left(3m_j^{\,2}/(j^2+j)-1\right) P_{n,j,m_j}(E) / \sum_{m_j=-j}^{j} P_{n,j,m_j}(E)$,[85] was also calculated and shown in Fig. 11 for various rotationally excited states of D_2, which can be directly compared with future experiments, as has been done for the D_2/Cu(111) system.[86] As expected, the rotational alignment is always positive, higher at lower energies but

decreases quickly to its minimum as the translational energy increases. This behavior, which can be attributed to the fact that the rotational motion parallel to the surface accelerates the dissociation of D_2, is consistent with the experimental findings for D_2/Cu(111) system[86] and theoretical predictions for several activated systems.[7-8, 85] Our results are qualitatively similar to experimental data on Cu(111) for (n=1, j=6) and (n=0, j=11), but in a different energy scale due to the difference in the barrier height, suggesting that these data may not be sensitive to the surface. In addition, it is interesting that $A_0^{(2)}$ for the j=2, 3, and 4 states are generally smaller than that for j=1. On the other hand, higher rotational states (j>6) show larger values of $A_0^{(2)}$ than that in the j=1 state, although the differences of $A_0^{(2)}$ among these higher rotational states are small. This overall trend is quite similar as what was found in H_2 dissociation on Cu(100) recently.[8]

Eichler et al. also found similar strong steric effects in H_2 dissociation on Ag(100),[29-30] namely H_2 with the helicopter rotation is much more reactive than that with the cartwheel rotation. Moreover, excitations to the first few low-lying rotational states of H_2 were also found to exhibit slight or no enhancement over the ground state, while further rotational excitations considerably increase the reactivity. These findings are all consistent with the current study.

IV. Conclusions

In this work, we report an accurate six-dimensional PES for H_2/D_2 dissociative chemisorption on Ag(111), based on a PIP-NN fit of about 4000 DFT points. The

PIP-NN approach enforces both the surface periodicity and the permutation symmetry for the molecule and provides a faithful representation of the DFT points (RMSD=2.5 meV). This is the first demonstration of the PIP-NN approach for a reactive molecule-surface system, and the results are very encouraging. This method is amenable to gas-surface PESs involving polyatomic molecules and future applications can thus be anticipated for dissociative chemisorption of methane[79] and water.[82, 87]

Full-dimensional quantum dynamics calculations on the PES were performed for both H_2 and D_2, and the resulting sticking probabilities are in general agreement with the measured values. The theory-experimental agreement is better at high collision energies, as the sticking coefficients at low collision energies are strongly influenced by the surface temperature, which was not included in the theoretical model. Nevertheless, the measured vibrational efficacy was reproduced and explained in terms of its coupling with the reaction coordinate at the transition state. In addition, the rotational and alignment effects were examined and found to be similar to H_2/D_2 dissociation on Cu(111) and Ag(100).

Acknowledgement: This work was supported by National Science Foundation (CHE-0910828), part of the calculations were performed at the National Energy Research Scientific Computing Center (NERSC). B.J. thanks Dr. Hongwei Song for some helpful discussions on the quantum dynamics code.

References:

1 K. Christmann, Surf. Sci. Rep. **9**, 1 (1988).
2 A. Gross, Surf. Sci. Rep. **32**, 291 (1998).
3 G.-J. Kroes, Prog. Surf. Sci. **60**, 1 (1999).
4 G.-J. Kroes, Phys. Chem. Chem. Phys. **14**, 14966 (2012).
5 P. Nieto, E. Pijper, D. Barredo, G. Laurent, R. Olsen, E. J. Baerends, G.-J. Kroes and D. Farias, Science **312**, 86 (2006).
6 C. Díaz, E. Pijper, R. A. Olsen, H. F. Busnengo, D. J. Auerbach and G.-J. Kroes, Science **326**, 832 (2009).
7 C. Diaz, R. A. Olsen, D. J. Auerbach and G. J. Kroes, Phys. Chem. Chem. Phys. **12**, 6499 (2010).
8 L. Sementa, M. Wijzenbroek, B. J. van Kolck, M. F. Somers, A. Al-Halabi, H. F. Busnengo, R. A. Olsen, G. J. Kroes, M. Rutkowski, C. Thewes, N. F. Kleimeier and H. Zacharias, J. Chem. Phys. **138**, 044708 (2013).
9 P. Avouris, D. Schmeisser and J. E. Demuth, Phys. Rev. Lett. **48**, 199 (1982).
10 P. T. Sprunger and E. W. Plummer, Phys. Rev. B **48**, 14436 (1993).
11 G. Lee and E. W. Plummer, Phys. Rev. B **51**, 7250 (1995).
12 X. L. Zhou, J. M. White and B. E. Koel, Surf. Sci. **218**, 201 (1989).
13 D. H. Parker, M. E. Jones and B. E. Koel, Surf. Sci. **233**, 65 (1990).
14 G. S. Lee, P. T. Sprunger, M. Okada, D. B. Poker, D. M. Zehner and E. W. Plummer, J. Vac. Sci. Technol. A **12**, 2119 (1994).
15 F. Healey, R. N. Carter and A. Hodgson, Surf. Sci. **328**, 67 (1995).
16 F. Healey, R. N. Carter, G. Worthy and A. Hodgson, Chem. Phys. Lett. **243**, 133 (1995).
17 H. Asada, Surf. Sci. **81**, 386 (1979).
18 J. M. Horne, S. C. Yerkes and D. R. Miller, Surf. Sci. **93**, 47 (1980).
19 C. F. Yu, K. B. Whaley, C. S. Hogg and S. J. Sibener, Phys. Rev. Lett. **51**, 2210 (1983).
20 C. F. Yu, K. B. Whaley, C. S. Hogg and S. J. Sibener, J. Chem. Phys. **83**, 4217 (1985).
21 L. Mattera, R. Musenich, C. Salvo and S. Terreni, Faraday Discuss. **80**, 115 (1985).
22 M. J. Murphy and A. Hodgson, Surf. Sci. **390**, 29 (1997).
23 M. J. Murphy and A. Hodgson, Phys. Rev. Lett. **78**, 4458 (1997).
24 C. Cottrell, R. N. Carter, A. Nesbitt, P. Samson and A. Hodgson, J. Chem. Phys. **106**, 4714 (1997).
25 Y.-W. Lin and G. Wolken, J. Chem. Phys. **65**, 3729 (1976).
26 U. Peskin and N. Moiseyev, J. Chem. Phys. **96**, 2347 (1992).
27 U. van Slooten, E. J. J. Kirchner and A. W. Kleyn, Surf. Sci. **283**, 27 (1993).
28 A. Eichler, G. Kresse and J. Hafner, Surf. Sci. **397**, 116 (1998).
29 A. Eichler, J. Hafner, A. Gross and M. Scheffler, Chem. Phys. Lett. **311**, 1 (1999).
30 A. Eichler, J. Hafner, A. Gross and M. Scheffler, Phys. Rev. B **59**, 13297 (1999).
31 Y. Xu, J. Greeley and M. Mavrikakis, J. Am. Chem. Soc. **127**, 12823 (2005).
32 A. Montoya, A. Schlunke and B. S. Haynes, J. Phys. Chem. B **110**, 17145 (2006).
33 A. B. Mohammad, K. H. Lim, I. V. Yudanov, K. M. Neyman and N. Rosch, Phys. Chem. Chem. Phys. **9**, 1247 (2007).
34 A. B. Mohammad, I. V. Yudanov, K. H. Lim, K. M. Neyman and N. Rosch, J. Phys. Chem. C

112, 1628 (2008).
35 T. Gomez, E. Florez, J. A. Rodriguez and F. Illas, J. Phys. Chem. C **115**, 11666 (2011).
36 Y. Kunisada and H. Kasai, J. Phys. Soc. Japan **82**, 023601 (2013).
37 B. Jiang and H. Guo, J. Chem. Phys. **141**, 034109 (2014).
38 G. Kresse and J. Furthmuller, Phys. Rev. B **54**, 11169 (1996).
39 G. Kresse and J. Furthmuller, Comp. Mater. Sci. **6**, 15 (1996).
40 P. E. Blöchl, Phys. Rev. B **50**, 17953 (1994).
41 G. Kresse and D. Joubert, Phys. Rev. B **59**, 1758 (1999).
42 H. J. Monkhorst and J. D. Pack, Phys. Rev. B **13**, 5188 (1976).
43 J. P. Perdew, K. Burke and M. Ernzerhof, Phys. Rev. Lett. **77**, 3865 (1996).
44 M. Methfessel and A. T. Paxton, Phys. Rev. B **40**, 3616 (1989).
45 H. Jónsson, G. Mills and K. W. Jacobsen, in *Classical and Quantum Dynamics in Condensed Phase Simulations*, edited by B. J. Berne, G. Ciccotti and D. F. Coker (World Scientific, Singapore, 1998).
46 G. Henkelman, B. P. Uberuaga and H. Jónsson, J. Chem. Phys. **113**, 9901 (2000).
47 C. M. Handley and P. L. A. Popelier, J. Phys. Chem. A **114**, 3371 (2010).
48 J. Behler, Phys. Chem. Chem. Phys. **13**, 17930 (2011).
49 L. M. Raff, R. Komanduri, M. Hagan and S. T. S. Bukkapatnam, *Neural Networks in Chemical Reaction Dynamics*. (Oxford University Press, Oxford, 2012).
50 M. T. Hagan and M. B. Menhaj, IEEE Trans. Neural Networks **5**, 989 (1994).
51 M. H. Beale, M. T. Hagan and H. B. Demuth, *Neural Network Toolbox™ 7 User's Guide*. (The MathWorks, Inc., Natick, MA, 2010).
52 B. Jiang and H. Guo, J. Chem. Phys. **139**, 054112 (2013).
53 J. Li, B. Jiang and H. Guo, J. Chem. Phys. **139**, 204103 (2013).
54 J. Ludwig and D. G. Vlachos, J. Chem. Phys. **127**, 154716 (2007).
55 Z. Xie and J. M. Bowman, J. Chem. Theo. Comp. **6**, 26 (2010).
56 B. J. Braams and J. M. Bowman, Int. Rev. Phys. Chem. **28**, 577 (2009).
57 J. Ischtwan and M. A. Collins, J. Chem. Phys. **100**, 8080 (1994).
58 L. M. Raff, M. Malshe, M. Hagan, D. I. Doughan, M. G. Rockley and R. Komanduri, J. Chem. Phys. **122**, 084104 (2005).
59 W. L. Hase, R. J. Duchovic, X. Hu, A. Komornicki, K. F. Lim, D.-H. Lu, G. H. Peslherbe, K. N. Swamy, S. R. V. Linde, A. Varandas, H. Wang and R. J. Wolf, Quantum Chemistry Program Exchange Bulletin **16**, 671 (1996).
60 X. Hu, W. L. Hase and T. Pirraglia, J. Comp. Chem. **12**, 1014 (1991).
61 J. Dai and J. C. Light, J. Chem. Phys. **107**, 1676 (1997).
62 D. Kosloff and R. Kosloff, J. Comput. Phys. **52**, 35 (1983).
63 D. T. Colbert and W. H. Miller, J. Chem. Phys. **96**, 1982 (1992).
64 D. H. Zhang and J. Z. H. Zhang, J. Chem. Phys. **99**, 5615 (1993).
65 J. C. Light and T. Carrington Jr., Adv. Chem. Phys. **114**, 263 (2000).
66 D. Lemoine, J. Chem. Phys. **101**, 10526 (1994).
67 G. C. Corey, J. W. Tromp and D. Lemoine, in *Numerical Grid Methods and Their Applications to Schroedinger's Equation*, edited by C. Cerjan (Kluwer, Dordrecht, 1993), pp. 1-23.
68 J. A. Flect Jr., J. R. Morris and M. D. Feit, Appl. Phys. **10**, 129 (1976).
69 T. Liu, B. Fu and D. H. Zhang, J. Chem. Phys. **139**, 184705 (2013).

70 J. C. Polanyi, Acc. Chem. Res. **5**, 161 (1972).
71 T. H. Liu, B. N. Fu and D. H. Zhang, Sci. China: Chem. **57**, 147 (2014).
72 H. F. Busnengo, A. Salin and W. Dong, J. Chem. Phys. **112**, 7641 (2000).
73 B. Jackson, in *Dynamics of Gas-Surface Interactions*, edited by R. D. Muino and H. F. Busnengo (Springer, Heidelberg, 2013).
74 A. Marashdeh, S. Casolo, L. Sementa, H. Zacharias and G.-J. Kroes, J. Phys. Chem. C **117**, 8851 (2013).
75 A. C. Luntz, J. Chem. Phys. **113**, 6901 (2000).
76 H. A. Michelsen, C. T. Rettner, D. J. Auerbach and R. N. Zare, J. Chem. Phys. **98**, 8294 (1993).
77 B. Jiang and H. Guo, J. Chem. Phys. **138**, 234104 (2013).
78 B. Jiang and H. Guo, J. Am. Chem. Soc. **135**, 15251 (2013).
79 B. Jiang, R. Liu, J. Li, D. Xie, M. Yang and H. Guo, Chem. Sci. **4**, 3249 (2013).
80 B. Jiang and H. Guo, J. Phys. Chem. C **117**, 16127 (2013).
81 B. Jackson, F. Nattino and G.-J. Kroes, J. Chem. Phys. **141**, 054102 (2014).
82 P. M. Hundt, B. Jiang, M. van Reijzen, H. Guo and R. D. Beck, Science **344**, 504 (2014).
83 D. A. McCormack, G.-J. Kroes, R. A. Olsen, E. J. Baerends and R. C. Mowrey, J. Chem. Phys. **110**, 7008 (1999).
84 G. R. Darling and S. Holloway, J. Chem. Phys. **101**, 3268 (1994).
85 J. Dai and J. C. Light, J. Chem. Phys. **108**, 7816 (1998).
86 H. Hou, S. J. Gulding, C. T. Rettner, A. M. Wodtke and D. J. Auerbach, Science **277**, 80 (1997).
87 B. Jiang, X. Ren, D. Xie and H. Guo, Proc. Natl. Acad. Sci. USA **109**, 10224 (2012).

Table I. Convergence of the activation energy with respect to the plane wave kinetic energy cutoff, number of *k* points, number of layers, and the size of the unit cell. All calculations were done using the PBE functional at a fixed transition state geometry which was obtained from CI-NEB optimization based on cutoff of 400 eV, 4×4×1 *k* points, four layers, and a 2×2 unit cell. The results obtained from previous studies are also included for comparison.

Cutoff (eV)	*k* points	Number of layers	Unit cell	E_a (eV)
350	4×4×1	4	2×2	1.15
400 [a]	4×4×1	4	2×2	1.16
450	4×4×1	4	2×2	1.16
500	4×4×1	4	2×2	1.16
400	6×6×1	4	2×2	1.14
400	8×8×1	4	2×2	1.14
400	4×4×1	5	2×2	1.08
400	6×6×1	5	2×2	1.18
400	8×8×1	5	2×2	1.16
400	4×4×1	4	3×3	1.15
400	6×6×1	4	3×3	1.17
340 [b]	18	4	2×2	1.11
340 [c]	6×6×1	5	2×2	1.13

[a] This work for the construction of potential energy surface.
[b] Ref. [31]. PW91 functional and Chadi-Cohen *k*-points were used in that work.
[c] Ref. [32]. PW91 functional was used in that work.

Table II. Parameters used in quantum dynamics calculations. Atomic units are used unless stated elsewhere.

Parameter	H_2(n=0, j=0)	D_2(n=0, j=0)
Grid range and size in (u, v)	u=v=(0-5.5628) N_u=N_v=14	u=v=(0-5.5628) N_u=N_v=14
Grid range and size in Z	Z=(0.2-15.0) $N_Z^{asy}=130,\ \ N_Z^{int}=35$	Z=(0.2-15.0) $N_Z^{asy}=160,\ \ N_Z^{int}=45$
Grid range and size in r	r=(0.5-6.0) $N_r^{asy}=6,\ \ N_r^{int}=28$	r=(0.5-6.0) $N_r^{asy}=8,\ \ N_r^{int}=32$
(j_{max}, m_{jmax})	(24, 16)	(26, 18)
Number of rotational basis	285	338
Initial wave packet	Z_0 = 14.0, δ = 0.30, E_0 = 1.2 eV	Z_0 = 14.0, δ = 0.30, E_0 = 1.2 eV
Adsorption potential	C_Z=0.10, C_r=0.10 Z_a=12.5, r_a=3.5	C_Z=0.10, C_r=0.10 Z_a=12.5, r_a=3.5
Flux position	3.2	3.2
Potential cutoff	4.0 eV	4.0 eV
Time step	15	10
Propagation time	15000	15000

Figure captions

Fig. 1, Schematic diagram of a feed-forward neural network.

Fig. 2. Coordinate system for describing the H_2 dissociation on the Ag(111) surface.

Fig. 3. Minimum energy path for H_2 dissociative chemisorption on Ag(111) obtained from CI-NEB. The red dashed line corresponds to the more favorable product with co-adsorbed H atoms at nearest fcc sites. The black solid line corresponds to the less favorable final state with co-adsorbed H atoms at the nearest fcc and hcp sites. Both reaction pathways yield the same transition state.

Fig. 4. Comparison between the MEP on the PIP-NN PES and directly calculated DFT energies at the MEP geometries. The corresponding activation energy (in eV) and vibrational frequencies (in cm^{-1}) are also given.

Fig. 5. Two-dimensional contour plots (with intervals of 0.2 eV) with the center of mass of H_2 fixed at the top, bridge, and fcc sites, with the angular coordinates fully relaxed. These sites are illustrated by the top view of the Ag(111) surface.

Fig. 6. Convergence of the dissociation probability with respect to the DFT points included in the PES fitting. The QCT results are shown in symbols and QD results in lines.

Fig. 7. Comparison of experimental and calculated sticking coefficients for H_2 (n=0, j=3) and D_2 (n=0 or 1, j=2) dissociative adsorption on Ag(111). The

logarithmic scale is used for the y-axis. The experimental data were extracted from the figures in Ref. 16 and Ref. 23.

Fig. 8. Comparison of calculated dissociation probabilities for several selected quantum states of H_2 and D_2 on Ag(111).

Fig. 9. Effect of the D_2 rotational excitation on the dissociation probability on Ag(111).

Fig. 10. Effect of the D_2 orientation on the dissociation probability on Ag(111).

Fig. 11. Rotational alignment parameters $A_0^{(2)}$ as a function of translational energy for the dissociative chemisorption of D_2 on Ag(111).

Fig. 1.

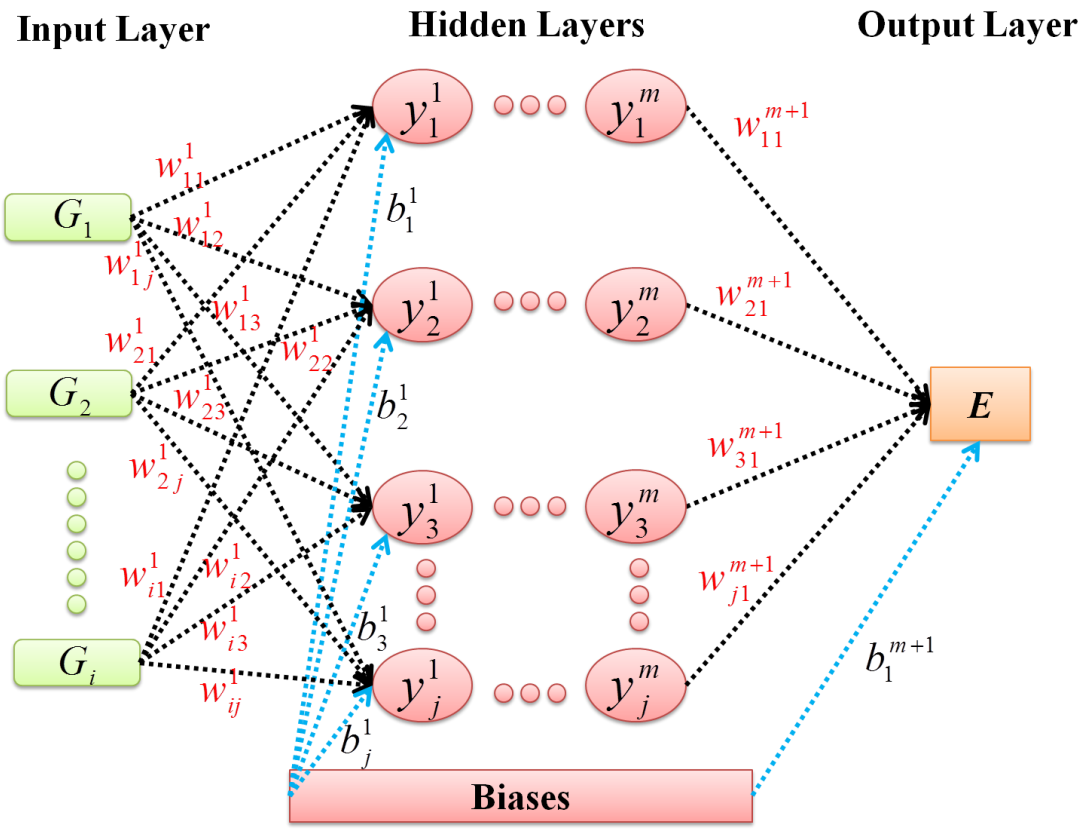

Fig. 2

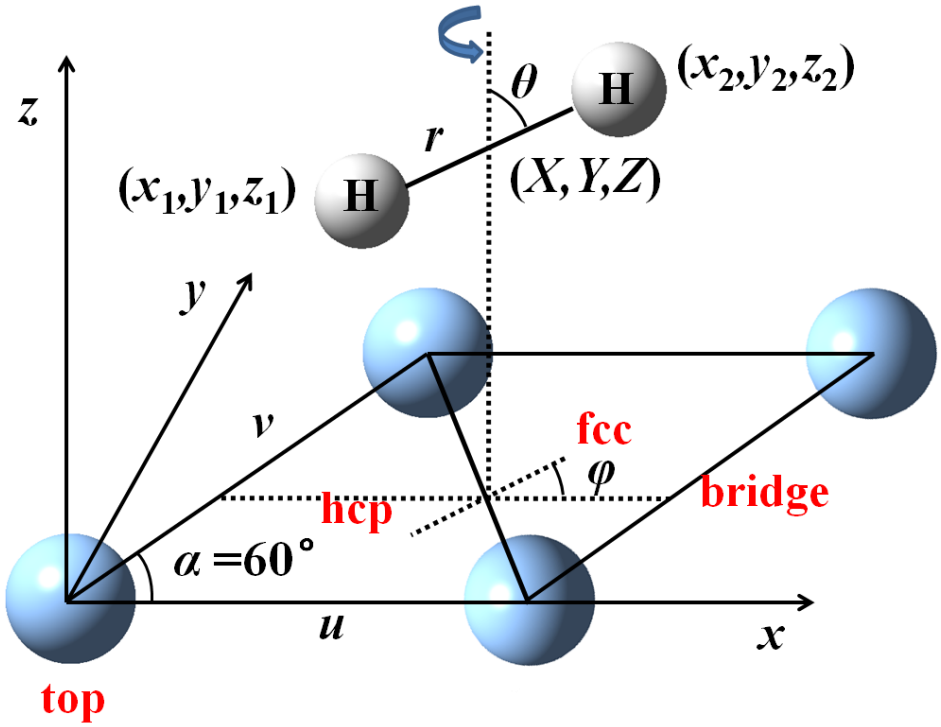

Fig. 3

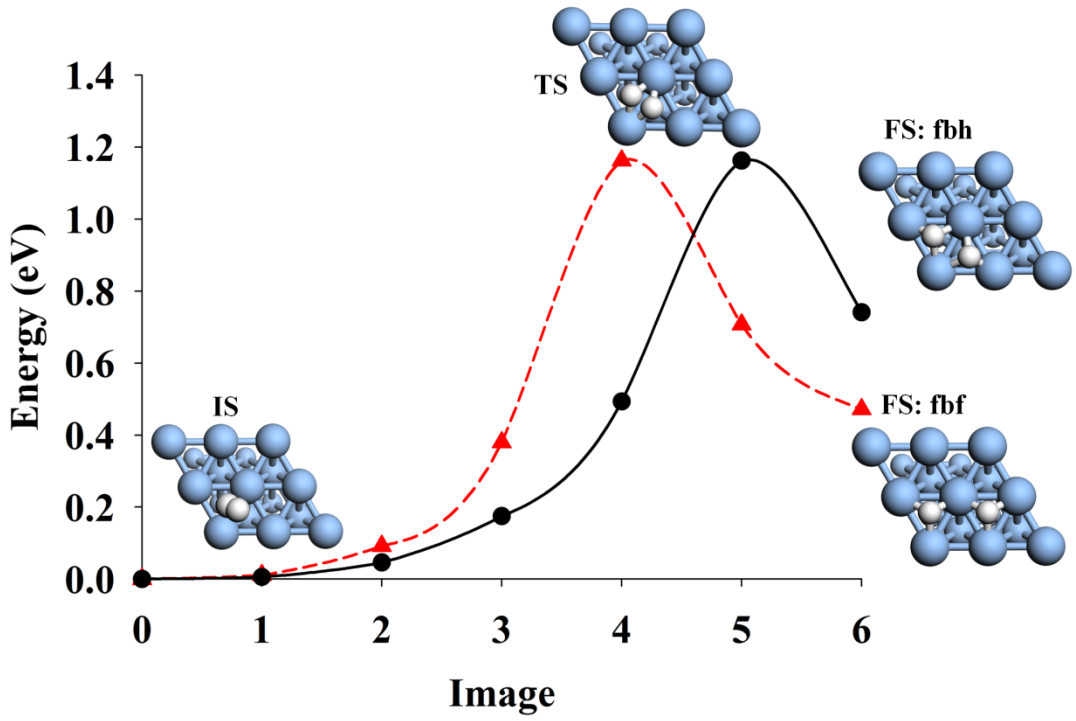

Fig. 4

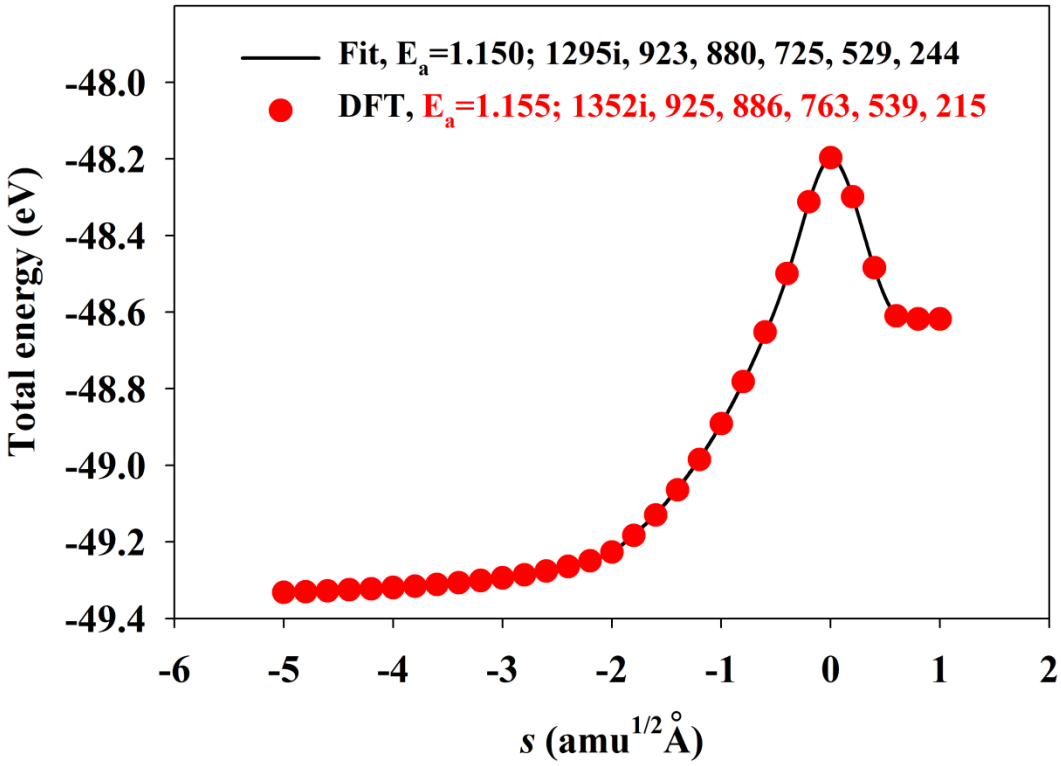

Fig. 5

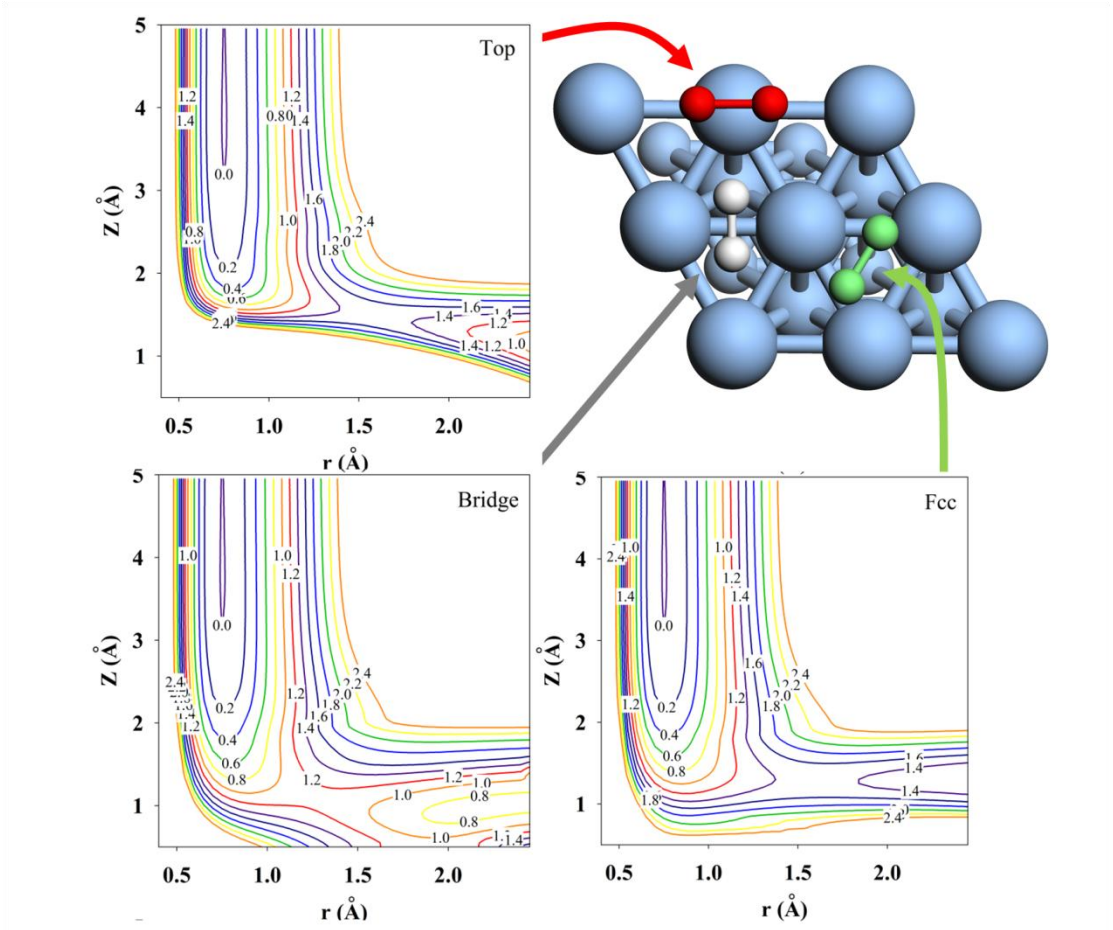

Fig. 6

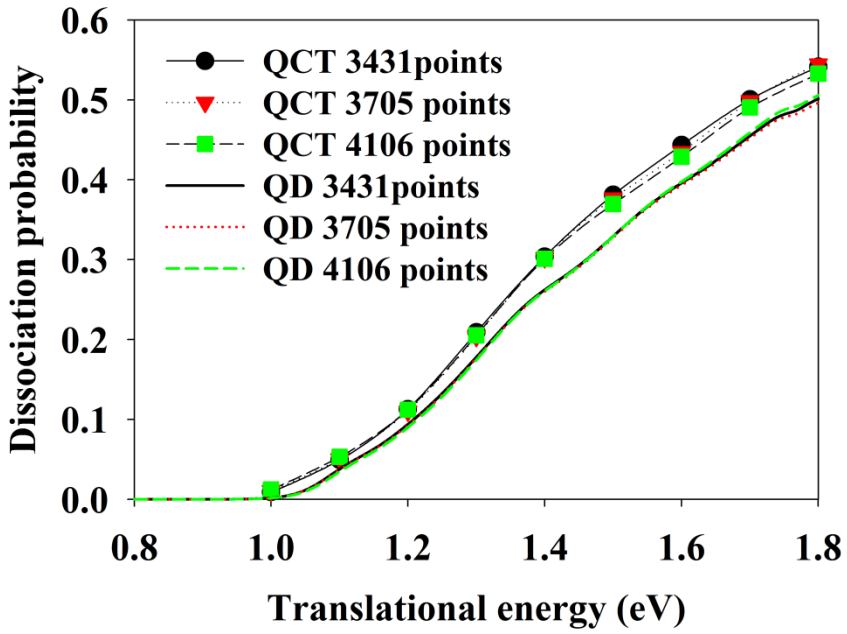

Fig. 7

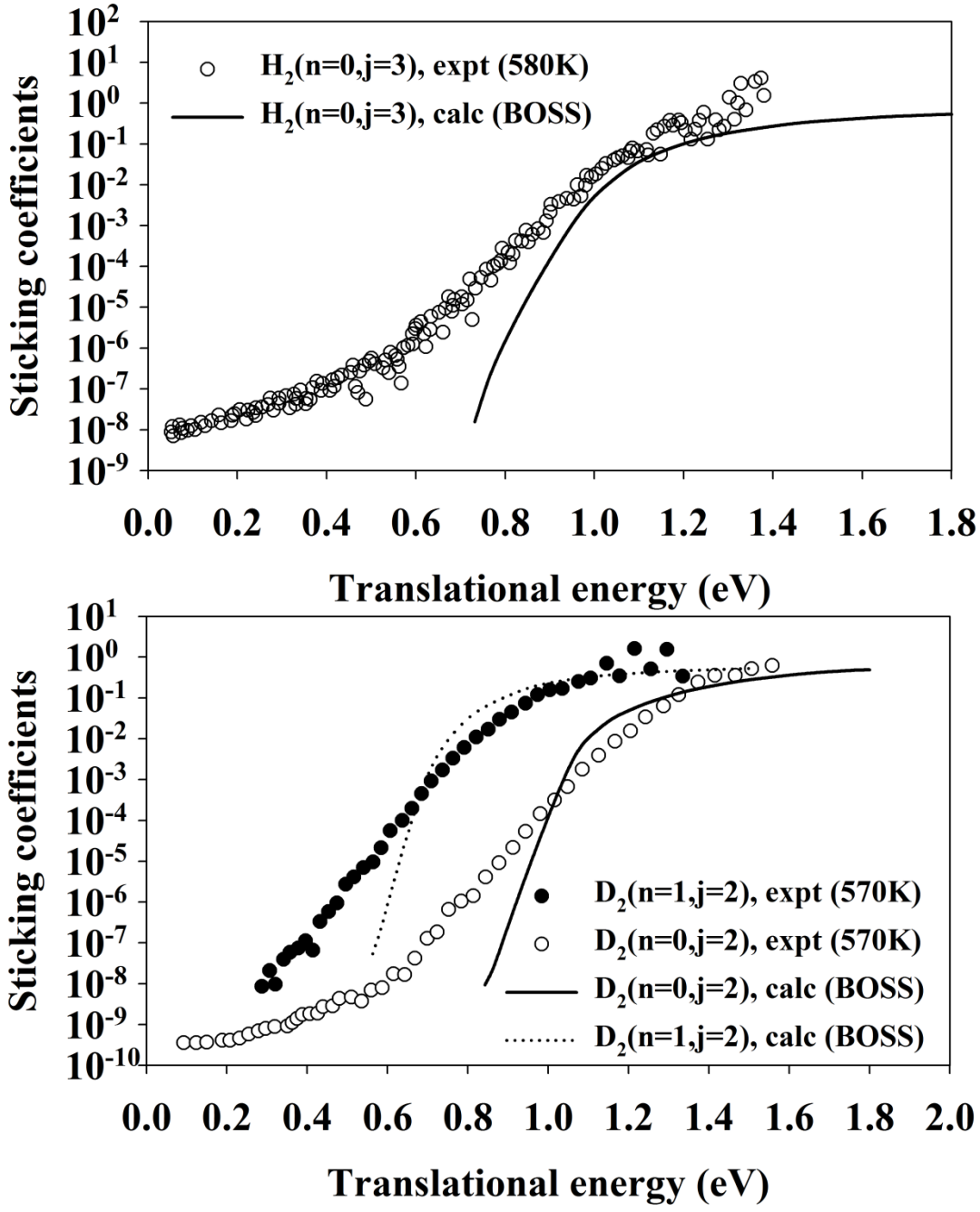

Fig. 8

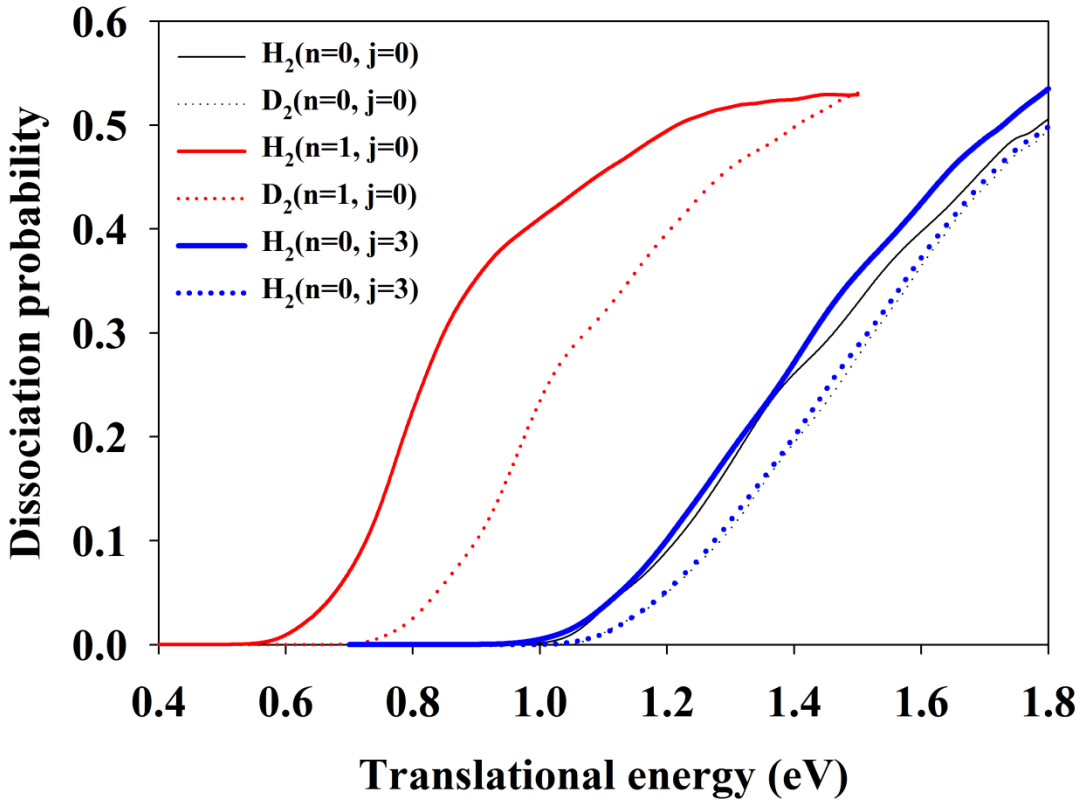

Fig. 9

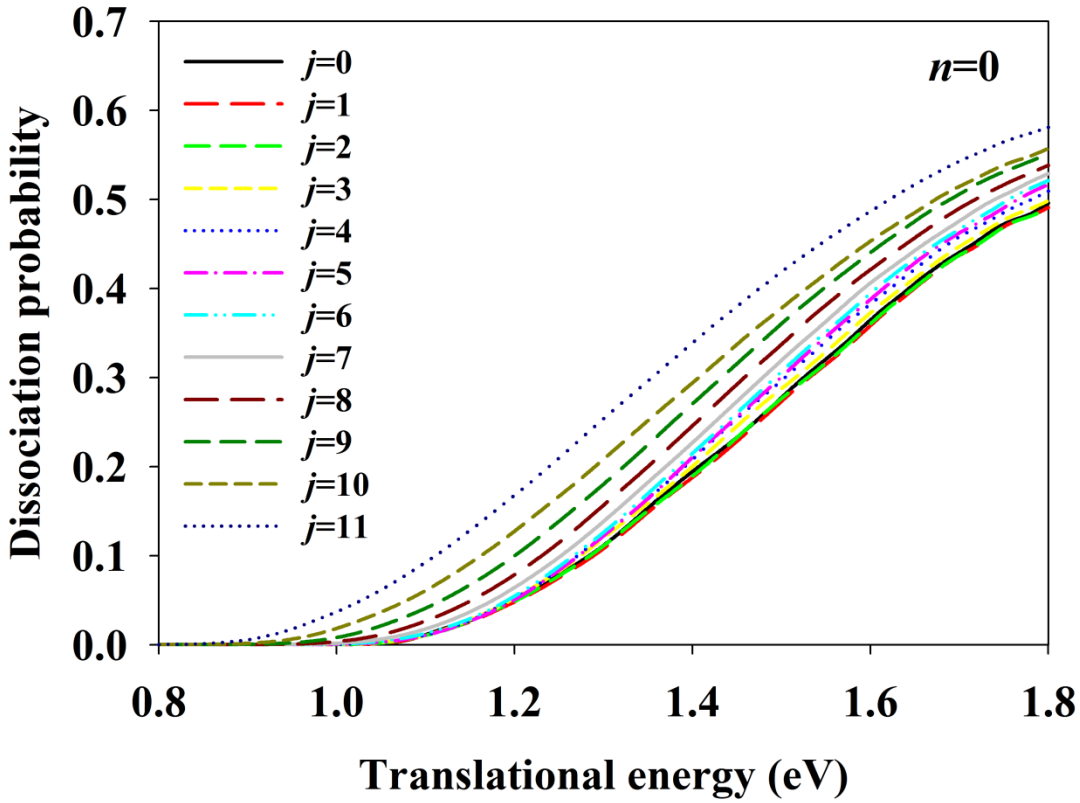

Fig. 10

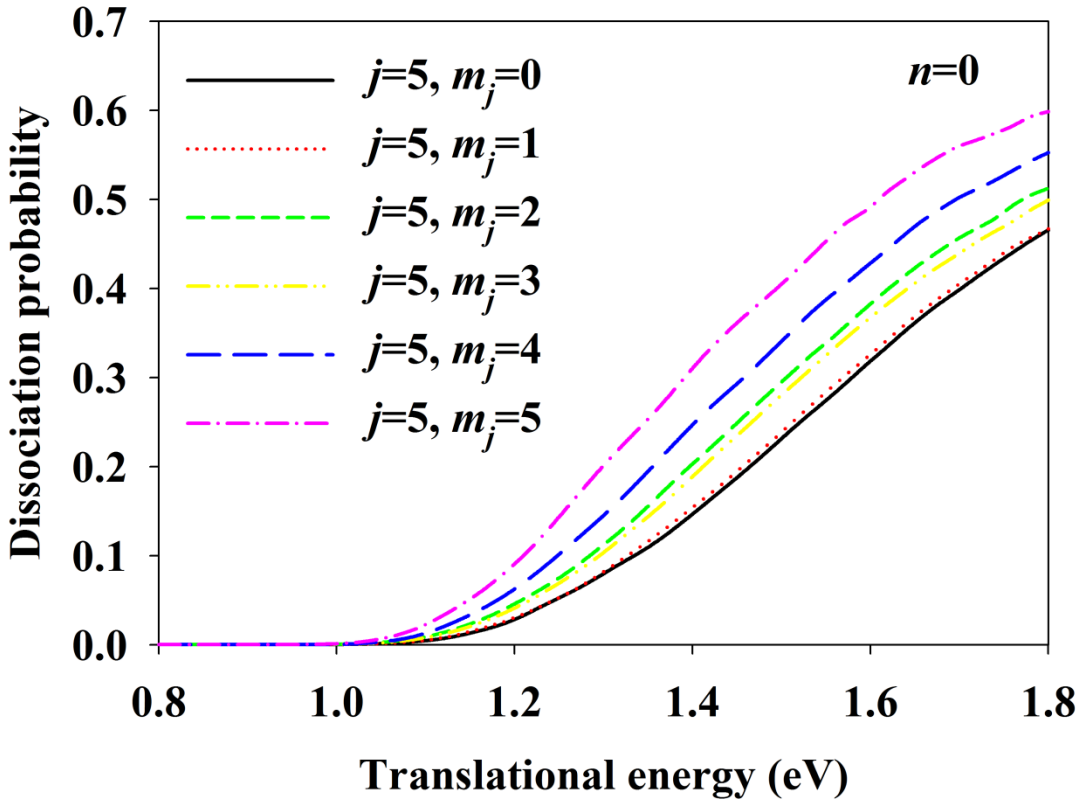

Fig. 11

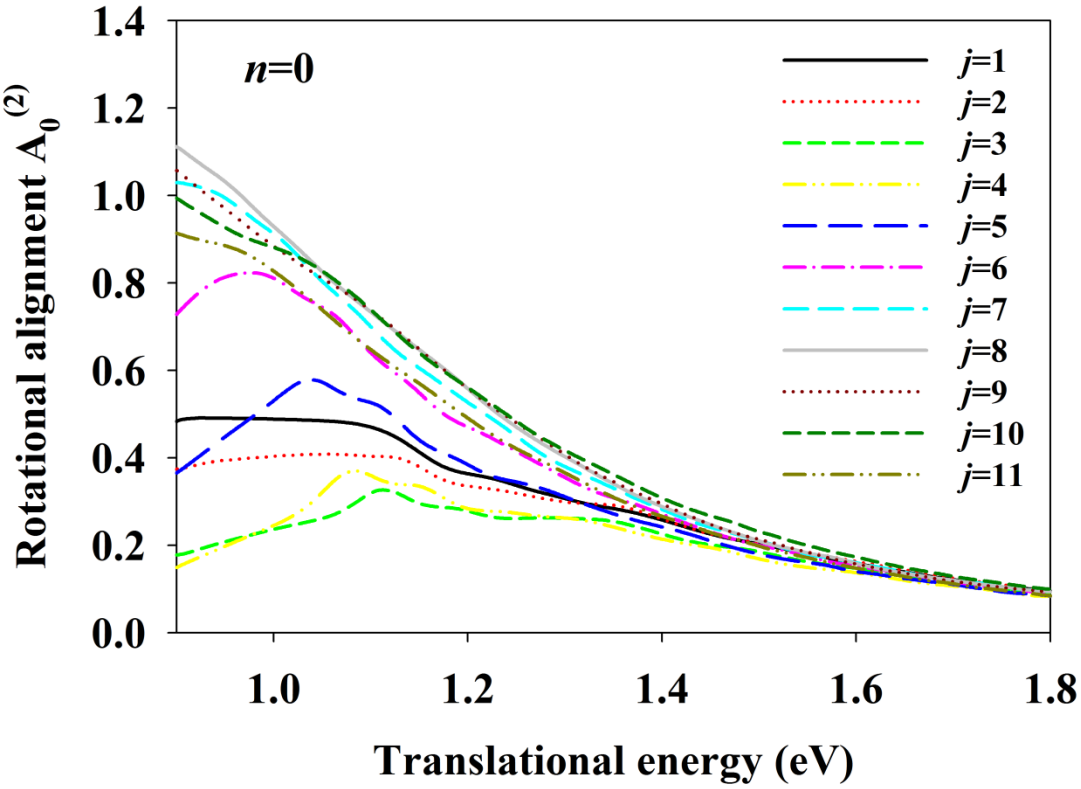

TOC graphic

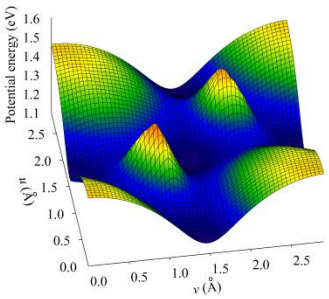

Quantum dynamics on a permutation invariant potential energy surface for H_2 dissociation on Ag(111) yield satisfactory agreement with experiment.